# Double-Layer Mediated Electromechanical Response of Amyloid Fibrils in Liquid Environment

M. P. Nikiforov,[†] G. L. Thompson,[‡] V. V. Reukov,[‡] S. Jesse,[†] S. Guo,[†] B. J. Rodriguez,[†,⊥] K. Seal,[†] A. A. Vertegel,[‡,*] and S. V. Kalinin[†,*]

[†]Oak Ridge National Laboratory, Oak Ridge, Tennessee 37831 and [‡]Clemson University, Department of Bioengineering, Clemson, South Carolina 29634. [⊥]Current address: University College Dublin, Ireland.

**ABSTRACT** Harnessing electrical bias-induced mechanical motion on the nanometer and molecular scale is a critical step toward understanding the fundamental mechanisms of redox processes and implementation of molecular electromechanical machines. Probing these phenomena in biomolecular systems requires electromechanical measurements be performed in liquid environments. Here we demonstrate the use of band excitation piezoresponse force microscopy for probing electromechanical coupling in amyloid fibrils. The approaches for separating the elastic and electromechanical contributions based on functional fits and multivariate statistical analysis are presented. We demonstrate that in the bulk of the fibril the electromechanical response is dominated by double-layer effects (consistent with shear piezoelectricity of biomolecules), while a number of electromechanically active hot spots possibly related to structural defects are observed.

**KEYWORDS:** amyloid · electromechanical coupling · double layer · PFM · SPM

Development of nanoscale systems capable of "acting" on the nanoscale is rapidly emerging as one of the prominent directions in nanoscience.[1−4] While silicon-based electronics is now projected to scale down to sub-10 nm level,[5] control of mechanical motion on these length scales presents an unresolved problem. A number of concepts based on optical,[6−11] chemical[2,12,13] (including biological ATP-fueled motors), and electrical powering[14,15] are being explored. Among all potential applications, electrically driven molecular machines are emerging as primary candidates due to the fast operation unlimited by achievable photon densities or diffusion of chemical species. These machines can be considered as a natural evolution of molecular electronic concept to include manipulation and motion.[2,16−21]

The examples include molecular nanocars[4] and molecular electromechanical machines. At the level of molecular assemblies, these include artificial muscles.[2,3] Despite the universally recognized role of electromechanical coupling in nanoscale systems manifesting themselves in changes of molecular shapes under electric field or during redox processes, the mechanisms of such phenomena until now have been inaccessible to experimental studies. The reason for this dearth of understanding is 3-fold and stems from (a) the need to establish a good electrical contact to molecule or molecular assembly, (b) the need to detect the resulting displacements and (c) the need for imaging in liquid environment. The latter requirement stems both from natural limitations inherent in unfolding spectroscopy[22] and the desire to mimic the natural functions of biological molecules and to control the performance at the molecular level. Thus, the tools to probe electromechanical activity on the molecular level are desperately needed.

In the past decade, significant progress in understanding of electromechanical coupling on the nanoscale has been achieved with the development of piezoresponse force microscopy (PFM).[23] Utilizing the intrinsic coupling between the electromechanical response of material and polarization order parameter, PFM has been broadly used to image domain structures down to *ca.* 3−10 nm resolution,[24−27] study the mechanisms for domain nucleation and growth,[28] and probe the mesoscopic mechanism for wall-defect interactions[29] and defect-mediated nucleation.[30,31] Recently PFM imaging of biological systems in ambient environment, including calcified tissues with ~sub-10 nm resolution has been demonstrated.[32] In parallel, PFM imaging[25] and switching[33] of ferroelectrics in liquids has been demonstrated. However, much lower electromechanical response of biological materials (1−3 pm/V, as compared to 10−1000 pm/V for perovskites) combined

with (a) much lower sensitivity of PFM in liquid due to viscous damping and added mass effects and (b) limitation on large voltage amplitudes have until now made the electromechanical imaging of biological and biomolecular systems in liquids impossible.

Here we report the measurements of electromechanical coupling in a prototypical biomolecular system—amyloid fibrils. Previously, the mechanical properties of fibrils[34−39] and their internal structure[40,41] have been studied in order to elucidate the mechanisms of their formation and their role in amyloidosis,[42,43] diabetes,[44−46] and Alzheimer's Disease.[47,48] In this work, we studied amyloid fibrils as a preparation step in understanding electromechanical coupling in live biological systems such as bacteria and cells. Specifically, we use the fibrils as a model soft system to study electromechanical coupling in liquid environment. In all studies to date, electromechanical response could not be unambiguously deconvoluted from the electrostatic interactions and contrast variations due to response variations in frequency dispersion of cantilever transfer function (*i.e.*, topographic cross-talk[49]). Here we use band excitation PFM (BE-PFM)[50] technique to measure electromechanical response of amyloid fibrils on mica and correlate it with the mechanical properties of the fibrils. We show that the mechanical properties of the fibril and the double layer at the fibril−water interface is responsible for the electromechanical response; however, a number of hotspots corresponding to regions with enhanced electromechanical activity can be observed.

## RESULTS AND DISCUSSION

**Electromechanical Imaging in Ambient and Liquid Environment.** The amyloid fibrils were prepared using standard protocols[34] as described in the Materials and Methods section. Electromechanical response was probed using piezoresponse force microscopy (PFM). In single frequency PFM, an oscillatory bias $V_{tip} = V_0 \sin(\omega t)$ is applied to the probe and electromechanical response is detected as a first harmonic of bias-induced tip displacement.[49] As a logical extension of single frequency PFM, band excitation PFM utilizes the electrical excitation performed using broadband excitation signal containing multiple excitation frequencies and the mechanical response measured over the same frequency band as excitation signal.[50,51] Both of these techniques were used in our work for the characterization of the electromechanical coupling in amyloid fibrils.

**Single Frequency Experiments.** Spatially resolved mechanical response of amyloid fibrils to electrical excitation in air and in water are compared in Figure 1. The width of the fibrils was found to

be approximately the same in air and water, while the height illustrated a profound change from ∼12 nm in water to ∼3 nm in air. There are several possible reasons for this discrepancy, including dehydration of the fibrils in air and mechanical deformation of the fibril due to the larger tip−surface and fibril−surface adhesion forces inevitable for imaging in air. The minimum tip−sample force for imaging in air is ∼100 nN, owing to the capillary forces between the tip and the surface. Imaging in liquid environment allows for better control of the tip−sample force. We used 0.15 nN tip−sample force for our liquid measurements. The difference in indentation force in air and liquid is most likely responsible for the change in height. The indentation depth on amyloid fibrils in air is about 20 nm, while in liquid it is only 0.25 nm (see Table 1), thus, the amyloid fibril should appear several tens of nm lower, when imaged in air comparing to one imaged in liquid. The differences in amplitude and in phase of PFM signal between the fibril and the substrate is clearly visible both in ambient and in liquid environment. In ambient (Figure 1a−c), amplitude and phase of PFM images show nonuniform contrast. The amplitude is larger on the left side of the fibril compared to the right side, and the phase is smaller on the right side of the fibril. There are at least two possible explanations for this behavior: the electromechanical properties of the fibril are nonuniform (left side has higher electromechanical response) or the error of the microscope's feedback and surface tracking increases when the tip approaches boundary between substrate and fibril. Experiments in liquid (Figure 1f,g) do not show such nonuniformity of electromechanical response indicating that left and right sides of the fibrils have similar electromechanical properties. In our experiments the tip approached the fibril from the left side (the scanning was done from left to right) leading to the increase in the microscope's feedback error on the left side of the fibril. Thus, it is logical to conclude that microscope's feedback error along with other sources of errors makes a significant contribution to the contrast in Figure 1b,c. In liquid the tip also scanned the area from left to right, and in this case the contrast in the amplitude and phase of PFM is similar on the left and right side of the amyloid fiber indicating that the contribution of the feedback error to the image is rather small. The almost 3 orders of magnitude decrease in tip indentation force for measurements in liquid com-

**TABLE 1. Mechanical and Electrical Properties of the Fibril and Mica,[59] Estimated Parameters of the Contact of Tip with the Surface**

| | air ($F_{indentation}$ = 100 nN) | | water ($F_{indentation}$ = 0.15 nN) | |
|---|---|---|---|---|
| Young's modulus | amyloid (160 MPa) | mica (150 GPa) | amyloid (160 MPa) | mica (150 GPa) |
| indentation depth (Hertzian model) | 19 nm | >0.20 nm | 0.25 nm | 0.0026 nm |
| contact radius (Hertzian model) | 28 nm | 2.8 nm | 3.2 nm | 0.32 nm |
| contact stiffness (Hertzian model) | 9 N/m | 840 N/m | 1.0 N/m | 96 N/m |
| dielectric function | ∼2 | 7 | ∼2 | 7 |

pared to ambient measurements is most likely responsible for this difference. PFM amplitude and phase show structural features within the fiber (Figure 1f,g). Comparison of the images of the fibril's topography and PFM amplitude and phase (Figure 1d−f) indicates that changes in electromechanical contrast follow the changes in fibril height. To give a proper explanation of the contrast in our electromechanical measurements, it is important to remember that PFM signal in is a convolution of several factors, most notably the electro-mechanical properties of the sample, electrostatic coupling between tip and the surface, contact mechanics of tip−surface junction, and cantilever mechanics.[52−54]

The dependence of single frequency piezoresponse as a function of the ac amplitude of tip voltage is shown for the mica and amyloid fiber measured in air (Figure 2a) and in liquid (Figure 2b). There are two mechanisms resulting in the linear dependence of the piezoresponse as a function of the ac amplitude of tip voltage, such as electromechanical properties of the sample or electrostatic coupling between tip and the surface.[55] In liquid electrostatic coupling should be screened at the distances larger than Debye length (~10 nm in water with pH 7 if no electrolytes are present), the fact that similar behavior of piezoresponse observed in liquid as well as in air suggests that the main part of the piezoresponse signal should come from the electro-mechanical properties of the sample.

In our experiments we measure the mechanical response of the tip coupled to the surface, which has large frequency dispersion with several apparent resonance frequencies, quality factors for these frequencies, etc. Mechanical resonances of the tip−surface system are determined by electromechanical properties of the sample (amyloid), tip−surface contact properties, and tip properties. All the factors listed above contribute to the PFM signal, and single frequency measurements do not provide enough information to determine the main factor responsible for PFM contrast. To establish the origins of the contrast in an amyloid fibril—the variation of elastic properties of electromechanical response—we
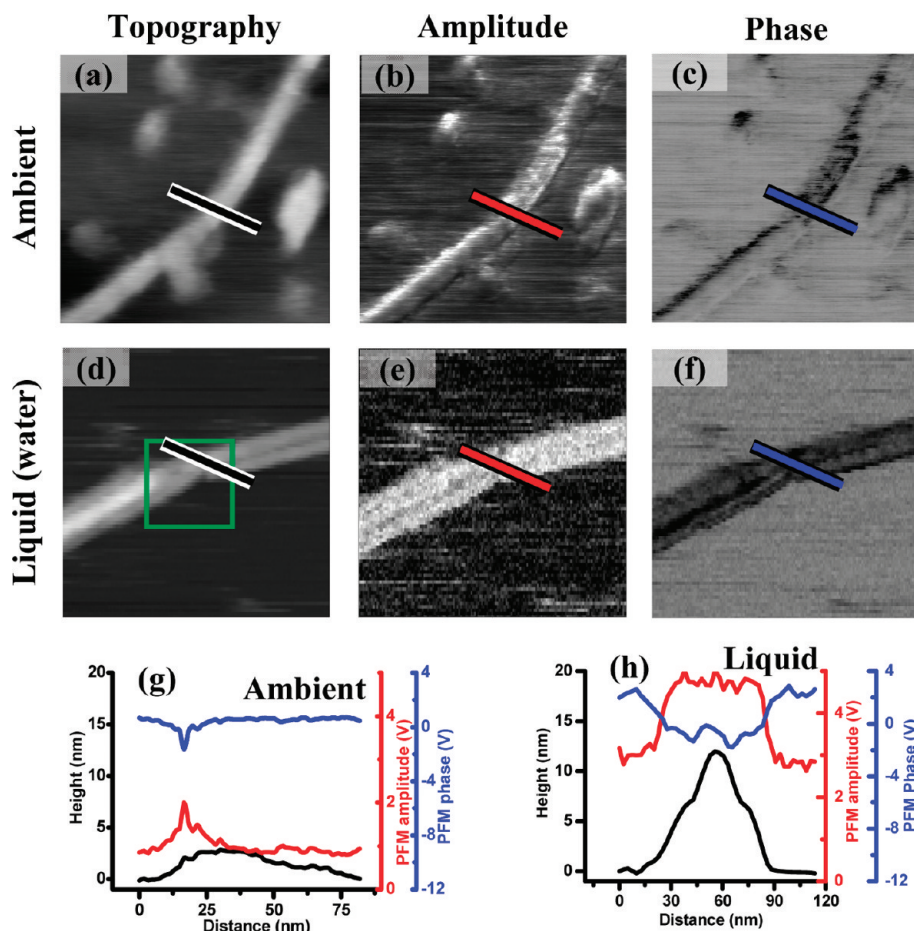


**Figure 1.** Spatially resolved measurements of electromechanical coupling between tip and amyloid-on-mica using single frequency PFM technique. Topography of the amyloid-on-mica sample measured by atomic force microscopy in air (a) and in water (d). Amplitude (b, e) and phase (c, f) of the mechanical signal excited by the AC electrical voltage applied to the tip measured in air (b, c) and water (e, f). All image sizes are 300 nm × 300 nm. Line profiles of the topography, amplitude, and phase images, as marked in air (g) and in water (h). The green box shows the area where broadband electromechanical response presented on Figure 4b−d was measured.
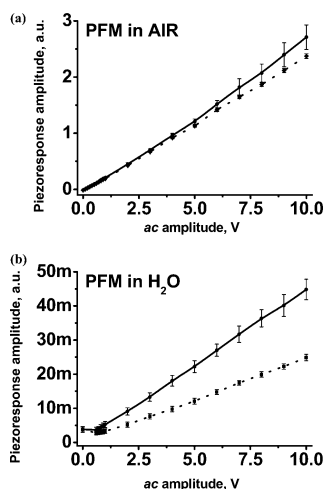


**Figure 2.** The strength of the single frequency PFM response as a function of the amplitude of tip voltage in air (a) and in liquid (b). Solid lines correspond to the PFM amplitudes on mica and dotted ones correspond to amyloid fiber.
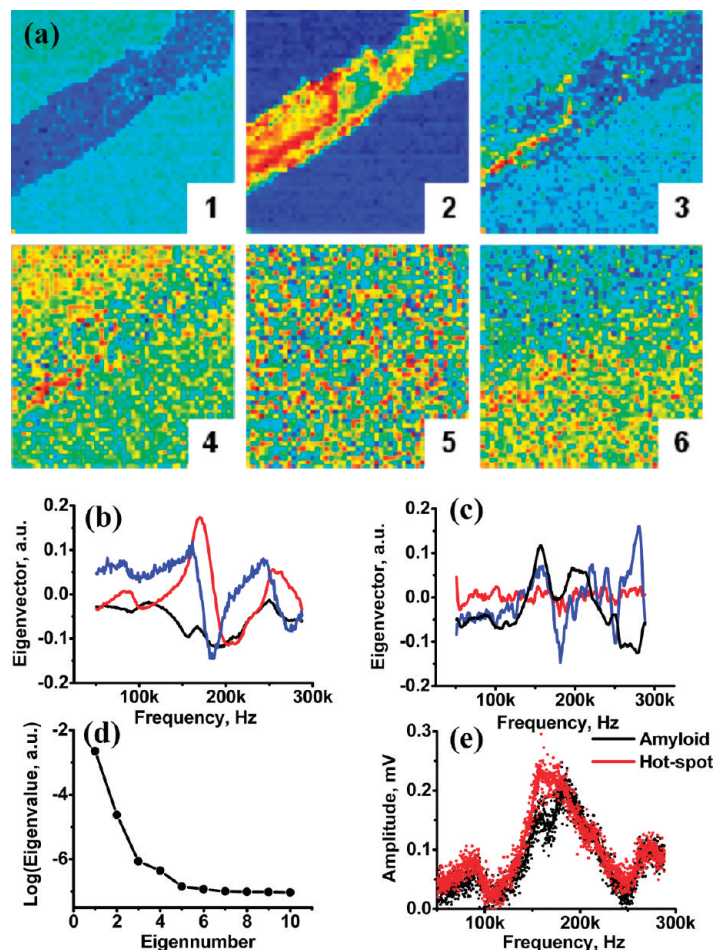
**Figure 3.** (a) Maps showing the spatial variations in magnitude of PCA components 1 through 9; (b) eigenvectors for PCA components 1 (black), 2 (red), 3 (blue); (c) eigenvectors for PCA components 4 (black), 5 (red), 6 (blue); (d) logarithm of the first 10 eigenvalues; (e) Amplitude spectra extracted from 5 "hot-spots" (red dots, solid red line is average response) and 5 points adjacent to them (black dots, solid black line is average response).

have used the band excitation PFM as described below. Band excitation PFM allows us to probe frequency dependence of the electromechanical response and, thus, to characterize the tip−surface contact resonance in much greater detail than single frequency measurements.

**Band Excitation PFM as a Method for Elimination of Topographical Cross-Talk in Electromechanical Coupling Measurements.** The main source of the ambiguity in electromechanical measurements is the change in elastic properties between the fibril and mica, which results in the variation of tip−surface spring constant and hence in the effective resonant frequency. For single frequency electromechanical measurements the amplitude of the response is a convolution of the electromechanical coupling signal and the error signal from the shift of the contact resonance spectrum. To deconvolute an electromechanical signal from a signal arising from the changes in contact resonance parameters, the whole frequency spectrum needs to be collected instead of a single frequency point.

Mechanical response of the amyloid-on-mica sample in a frequency range around tip−surface contact resonance (50−280 kHz) was collected using the band-excitation method. The mechanical resonance was excited by a broadband (50−280 kHz) electrical signal of constant amplitude of 10 V (Materials and Methods). Figure 3a shows the electromechanical response of amyloid fibrils on mica. This response has a complicated structure with several resonance peaks that can be analyzed using statistical methods[56] or functional fit.

*Multivariate Statistical Analysis of BE Data.* The band excitation method allows collecting full amplitude- and phase-frequency response spectra at each point of the sample surface. As is usual for imaging in liquids, the response in the 50−300 kHz range contains multiple response peaks related to both intrinsic materials responses and nonidealities in the cantilever and holder transfer functions. To avoid the uncertainty in data interpretation and establish the veracity of the fitting procedure, we analyze spectroscopic BE data using principal component analysis (PCA).[56−58] The spectroscopic image of $N \times M$ pixels formed by spectra containing $P$ points is represented as a superposition of the eigenvectors $w_j$,

$$PR_i(\omega_j) = a_{ik} w_k(\omega_j) \qquad (1)$$

where $a_{ik} \equiv a_k(x,y)$ are position-dependent expansion coefficients, $PR_i(t_j) \equiv PR(x,y,\omega_j)$ is the image at a selected time, and $\omega_j$ are the discrete frequencies at which response is measured. The eigenvectors $w_k(\omega)$ and the corresponding eigenvalues $\lambda_k$ are found from the covariance matrix, $\mathbf{C} = \mathbf{A}\mathbf{A}^T$, where $\mathbf{A}$ is the matrix of all experimental data points $\mathbf{A}_{ij} = PR_i(\omega_j)$, that is, the rows of $\mathbf{A}$ correspond to individual grid points ($i = 1, ..., N \cdot M$), and the columns correspond to frequency points, $j = 1, ..., P$. The eigenvectors $w_k(w_j)$ are orthogonal and are chosen such that the corresponding eigenvalues are placed in descending order, $\lambda_1 > \lambda_2 > ...$

The spatial maps of the first six PCA components (loading maps) of the piezoresponse data arrays and the corresponding eigenvectors and eigenvalues are shown in Figure 3a. Notably, the first three loading maps show pronounced spatial structure with the varying level of details. The PCA 1 map shows strong variation of contrast between the fibril and the surrounding mica but very small contrast within the fibril. The PCA 2 map shows both strong variation of contrast between fibril and mica, and significant and clearly visible features within the fibril. Finally, the PCA 3 map shows a number of visible "hot spots" within the fibril but only limited contrast between fibril and mica. These spots are also visible in the PCA 4 map. In comparison, the PCA 5 map is essentially structureless, and PCA 6 map shows the slope drift from the top left to bottom right corner of the image. The shape of $\lambda_k(k)$ dependence (Figure 3d) indicates that the first 3 PCA components

contain the ~90% of significant information within the 3D spectral image, whereas remaining $P - 5$ components are dominated by noise. Based on the behavior of the Figure 3b,c plots and spatial correlations in the loading maps, the PCA maps 1−4 and 6 contain the significant information within the image.

Note that the PCA analysis is a purely statistical method and does not employ any assumption regarding the underlying physical behavior, ensuring its fidelity. However, in many cases the approximate interpretation of the data can be achieved based on the shape of corresponding eigenvector, $w_i(\omega_j)$, and simple physical model.[56] The first eigenvector represents the gross difference in the electromechanical response amplitude between fibril and mica (note the similarity between the eigenvector and the overall response). The second and third eigenvector are reminiscent of the derivatives of the first one and can be identified with the resonance frequency shift, that is, variation of stiffness within the fibril. The fifth eigenvector is essentially noise-like, as expected. Finally, the sixth eigenvector represents the creep of resonance frequency (e.g., due to the changes in hydrodynamic damping induced by the changes in tip−surface separation).

The PCA analysis allows establishing the presence of the pints with anomalous response ("hot spots" in PCA 3 and 4 maps). The corresponding amplitude−frequency curves averaged over these locations are shown in Figure 3e, demonstrating the significant increase of electromechanical response amplitude in these regions.

*Functional Fitting.* To quantify the BE data, we use a damped harmonic oscillator (DHO) model, which provides a reasonable fit for each of the resonance peaks as well as a clear physical meaning of all parameters calculated from the spectra; we also performed principle component analysis of the experimental data (for the protocol see ref 56) and found that the system has three linearly independent variables similar to the number of variables DHO has. The DHO model (eq 2) describes the movement of an object with mass $m$ at the end of a system of a spring and a damper connected in parallel as a function of time after the object was displaced from the equilibrium position:

$$\frac{d^2x}{dt^2} + 2\xi\omega_0\frac{dx}{dt} + \omega_0^2 x = 0 \qquad (2)$$

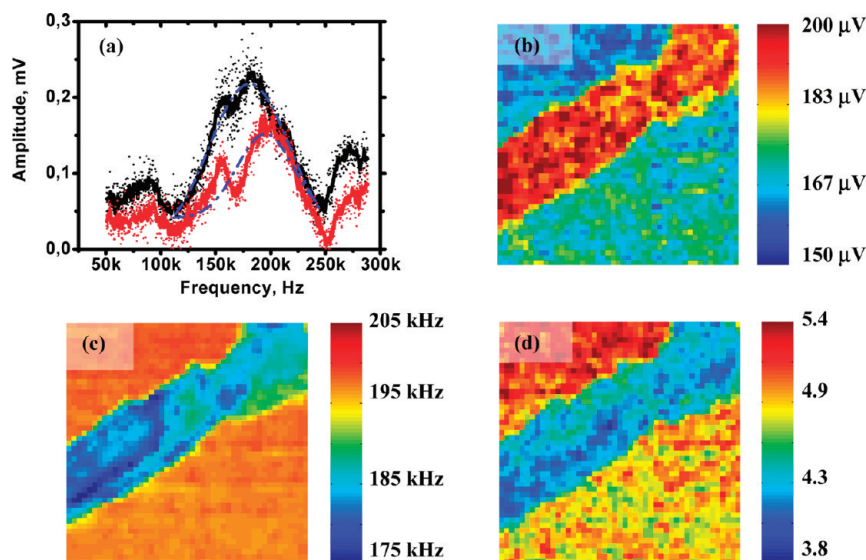where $m$ is the mass of the object, $x$ is the displace-



Figure 4. (a) Examples of the broad frequency electromechanical response (red is typical spectrum of mica, black is typical spectrum for amyloid fiber). Blue lines are the fit of the spectrum using damped harmonic oscillator model. Spatially resolved maps of the amplitude (b), resonance frequency (c), and quality factor (d) of electromechanical response calculated as damped harmonic oscillator fit of the frequency spectra.

ment of the mass, $t$ is time, $\omega_0$ is the angular resonance frequency ($\omega_0 = (k/m)^{1/2}$), $\xi$ is the damping ratio ($\xi = c/2m\omega_0$), $k$ is stiffness of the spring, and $c$ is mechanical losses in the system (damping coefficient). In band excitation PFM the driving electrical band of frequencies is chosen to be around the mechanical resonance of the tip−surface system. Thus, the amplitude and phase spectra as a function of frequency provide characteristic parameters, such as resonance amplitude, resonance frequency, and quality factor of the tip−surface resonance. Such an experimental setup and analysis technique allows us to measure parameters of the electromechanical coupling between the tip and the sample. Note that the DHO model has three independent parameters, which is close to the estimated by the PCA analysis (strong variability in PCA 1−3 maps, except for "hot spot" regions).

The resonance frequency of the tip−sample contact is proportional to the contact stiffness, which in turn is related to the Young's modulus and the contact area:

$$k_2 = 2aY \qquad (3)$$

where $k_2$ is the contact stiffness, $a$ is the radius of the contact, and $Y$ is the indentation modulus of the material.

In this description, the resonance amplitude of the electromechanical coupling is a measure of electromechanical coupling free from topographical artifacts, because the changes in contact stiffness are compensated by the resonance frequency tracking. Quality factor is the measure of energy dissipation during the conversion of electrical energy into mechanical energy. Finally,

resonance frequency is a measure of the local elastic properties of material.

Spatially resolved measurements of resonance frequency (determined as functional fit of each spectrum with single damped harmonic oscillator) (Figure 4c) show that the resonance frequency of tip−surface contact varies over a wide range (∼15 kHz) within the amyloid fibril, while the amplitudes of piezoelectric responses of the amyloid fibril is almost constant (Figure 4b).

Experiment shows that tip−mica and tip−amyloid contacts have resonance frequencies and quality factors of 195 kHz and 4.9, and 185 kHz and 4.4, respectively. Such a small difference in quality factor (less than 15%) of amyloid fibril and mica suggests that the mechanism for electromechanical coupling is the same for these two materials. Under the experimental conditions the change in quality factor alone cannot explain the change in resonance frequency (in DHO model the resonance frequency and the quality factor are connected by the equation $f_{res} = f_0(1 - 1/Q^2)^{1/2}$), thus, the change in contact stiffness definitely affects the resonance frequency.

Table 1 shows indentation depth, contact radius, and contact stiffness for ambient and liquid measurements estimated using the Hertzian model of the tip−surface contact using tip radius of 40 nm, Poisson ratio of 0.3 for mica and amyloid, and indentation forces of 100 nN (ambient) and 0.15 nN (liquid). The Hertzian model was used as the simplest model for tip−surface contact with the least amount of free parameters. All parameters used in modeling are close to those used in experiment. The large differences in Young's modulus and contact stiffness between amyloid and mica explain the difference in observed contact resonance frequencies. Also the large indentation depth of the amyloid fibril in air explains the difference in the measured height of the fibrils in air and liquid.

**The Nature of Electromechanical Coupling in Amyloid−Mica System.** Both mica and amyloid fibers are materials with small intrinsic piezoelectric effect. Mica is centrosymmetric, and hence bulk piezoeffect is zero, although surface electromechanical responses are possible.[60] In amyloid fibrils, as in other biomolecular systems, the shear piezoeffect is expected.[61] In this case for ideal fibril orientation the vertical PFM response is expected to be zero, with defects and structural irregularities providing regions with nonzero signal.

In addition to materials-related mechanisms, reproducibly observed electromechanical couplings between the metal-coated tip and amyloid-and-mica surface may involve (i) double layer coupling, (ii) dipole reorientation.

The exact equation for double layer coupling[62] model for electromechanical response $d_{33}$ (the quantitative measure of the piezoelectric response in the direction perpendicular to the sample surface) can be adopted from the electromechanical response of electret films[63,64] with the sample and one layer of charges (Figure 5).

$$d_{33}(\text{sample}) \cong$$
$$\frac{\varepsilon_{sample}\varepsilon_{water}(h_{sample} + h_{DL})h_{sample}h_{DL}\sigma_{sample}}{Y_{sample}(\varepsilon_{water}h_{sample} + \varepsilon_{sample}h_{DL})^2} \quad (4)$$

Here $\varepsilon$ is the permittivity of the solid material, $h_{sample}$ is the thickness of sample, $h_{DL}$ is the thicknesses of double layer, $\sigma$ is the charge density of the double layer, and $Y$ is the Young's modulus of the solid.

**Relationship between Measured Parameters and Parameters of the Model.** In our experiment absolute values of electromechanical amplitude are proportional to $d_{33}$. The absolute value of $d_{33}$ calculated from the experimental data is difficult to quantify;[65] however, relative changes in $d_{33}$ measured with atomic force microscopy on one sample are very accurate. Thus, the ratio of $d_{33}$(amyloid) to $d_{33}$(mica) can easily be extracted from spatially resolved maps of amplitude of electromechanical resonance (Figure 6a). This ratio [$d_{33}$(amyloid)/$d_{33}$(mica)] can also be calculated using:

$$\frac{d_{33}(\text{amyloid})}{d_{33}(\text{mica})} \cong$$
$$\frac{\sigma_{amyloid}\varepsilon_{amyloid}}{\sigma_{mica}\varepsilon_{mica}} \frac{(\varepsilon_{water}h_S + \varepsilon_{mica}h_{DL})^2}{(\varepsilon_{water}h_S + \varepsilon_{amyloid}h_{DL})^2} \frac{Y_{mica}}{Y_{amyloid}} \quad (5)$$

Since the thickness of the sample is much larger than the thickness of the double layer and eq 5 can be simplified assuming $h_S \rightarrow \infty$ limit (eq 6),

$$\frac{d_{33}(\text{amyloid})}{d_{33}(\text{mica})} \cong \frac{\sigma_{amyloid}\varepsilon_{amyloid}}{\sigma_{mica}\varepsilon_{mica}} \frac{Y_{mica}}{Y_{amyloid}} \quad (6)$$

the Young's modulus of the material can be calculated from the measured resonance frequency as Jesse et al. have already shown.[66] Different contact resonances can be used to calculate contact stiffness as a function of frequency:

$$f^i_{res} \cong \left(1 - b_i\frac{k_1}{k_2}\right)f_{0bound} \quad (7)$$

where $f_{res}$ is the resonance frequency of the tip−surface contact, $i$ is the order of the resonance, $f_{0bound}$ is the resonance frequency of the tip in contact with infinitely stiff surface (this parameter depends only on the cantilever), $k_1$ is the spring constant of the cantilever, $k_2$ is the contact stiffness. The coefficients for the first five contact resonances were calculated ($b_1 = 7.7$, $b_2 = 36.5$, $b_3 = 80.4$, $b_4 = 144.9$, $b_5 = 230.8$, ...) on the basis of the numerical analysis of contact resonance given in ref 51.

Contact stiffness of the material in the first approximation is related to the Young's modulus and contact area as $k_2 = 2aY$, where $a$ is the radius of the contact. After simple algebra, relationship for Young's modulus as
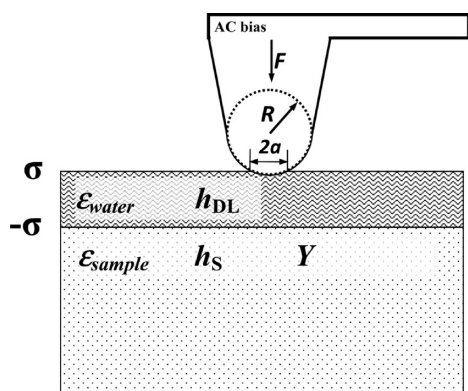
Figure 5. The schematics of the double layer model.

a function of resonance frequency can be deduced:

$$Y \cong \frac{b_i k_1}{2a}\left(\frac{f_{0\text{bound}}}{f_{0\text{bound}} - f_{\text{res}}}\right) \qquad (8)$$

Substituting eq 8 into eq 6 we obtain

$$\frac{d_{33}(\text{amyloid})}{d_{33}(\text{mica})} \cong \frac{\sigma_{\text{amyloid}}\varepsilon_{\text{amyloid}}}{\sigma_{\text{mica}}\varepsilon_{\text{mica}}}\frac{a_{\text{mica}}}{a_{\text{amyloid}}}\left(\frac{f_{0\text{bound}} - f_{\text{mica}}}{f_{0\text{bound}} - f_{\text{amyloid}}}\right) \qquad (9)$$

Equation 9 provides a functional relationship between electromechanical response and material stiffness assuming double layer mediated electromechanical response in the system. To test whether the electromechanical response is described completely by the elasticity effect, we calculate spatially resolved maps of the ratio $d_{33}$(amyloid)/$d_{33}$(mica) from amplitude of electromechanical response (left side of eq 9) and from resonance frequency (right side of eq 9).

**Modeling Electromechanical Contrast Image.** Figure 6a was created by dividing the spatially resolved values of electromechanical amplitude (Figure 4b) by the average value of electromechanical amplitude of mica (~150 μV).

Modeling of the electromechanical coupling ratio from resonance frequency (Figure 6b) was done as follows:

(1) The mask of the image with clear differentiation between mica (blue) and amyloid fiber (red) was created (Figure 6c).

(2) The ratio of electromechanical coupling coefficients on mica area was calculated according to

$$\frac{d_{33}}{d_{33}(\text{mica})(x, y)} \cong \left(\frac{f_{0\text{bound}} - f_{\text{image average}}}{f_{0\text{bound}} - f_{\text{mica}}(x, y)}\right) \qquad (10)$$

where $f_{0\text{bound}}$ is the fitting parameter, $f_{\text{image average}}$ is the average resonance frequency of the image ($f_{0\text{bound}} = 242$ kHz, $f_{\text{image average}} = 195.5$ kHz).

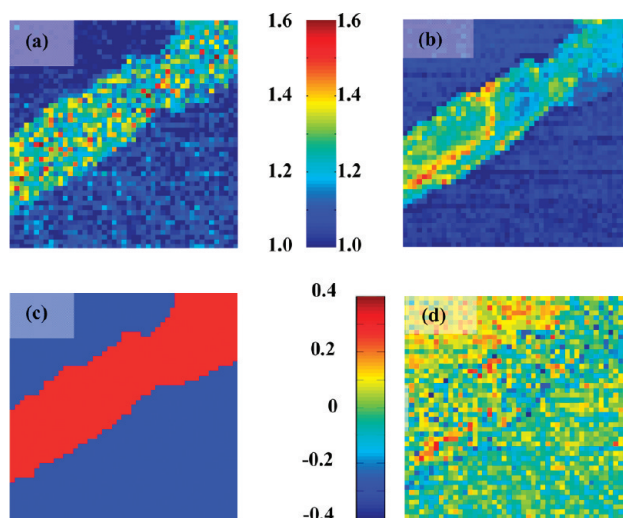(3) The ratio of piezoelectric coefficients on amyloid fiber was calculated according to



Figure 6. (a) Experimentally measured ratio of $d_{33}$ to $d_{33}$(mica). (b) Modeled ratio of $d_{33}$ to $d_{33}$(mica) assuming double layer coupling model. (c) The attribution of mica and amyloid fiber on the image. (d) The difference map between modeled and experimentally measured ratios.

$$\frac{d_{33}(\text{amyloid})(x, y)}{d_{33}(\text{mica})} \cong \left(\frac{f_{0\text{bound}} - f_{\text{amyloid}}(x, y)}{f_{0\text{bound}} - f_{i\text{mage average}}}\right) \qquad (11)$$

where where $f_{0\text{bound}}$ is the fitting parameter, $f_{\text{image average}}$ is the average resonance frequency of the image ($f_{0\text{bound}} = 242$ kHz, $f_{\text{image average}} = 195.5$ kHz).

The values for $f_{\text{mica}}$ and $f_{\text{amyloid}}$ are taken from Figure 2c; $f_{0\text{bound}}$ was adjusted to minimize the difference between modeled image and experimental map.

To understand the quality of the fit, a spatially resolved difference map was created (Figure 6d). The fitting error is less than ±15%; also no apparent contrast on the difference image can be seen. This proves that the difference in electromechanical coupling between mica and amyloid fiber can be explained by the difference in the indentation moduli between those two materials. It also validates the use of double layer model for the description of the electromechanical contrast in the amyloid-on-mica system.

The reconstructed map in Figure 6d exhibits a number of the "hot spots" of high electromechanical activity. These hot spots represent correlated response at several adjacent locations and thus cannot be attributed to pure noise response. The comparison with topography illustrates their correlation with the topographic inhomogeneities. Because the predominant piezoelectric coupling in these materials is shear, the disruption of fibril structure can create the regions of high electromechanical response, suggesting a possible explanation for observed phenomenon.

## CONCLUSIONS

In this work we unraveled an origin of the electromechanical coupling observed on mica and amyloid fi-

bers. The use of piezoresponse force microscope with broadband electrical excitation of the tip and signal detection allows for reliable study of electromechanical coupling in amyloid fibrils. Also, this methodology is directly transferrable to molecular systems, molecular assemblies, and biological systems, which are crucial parts of the nanorobot devices for minimally invasive

surgeries,[67,68] body functions monitoring,[69,70] *etc*. The electromechanical response of the double layer is responsible for this effect with the Young's modulus of the material being the main parameter that determines the magnitude of electromechanical coupling. The double layer effect on electromechanical coupling extends to the other soft materials, such as polymer brushes, *etc*.

## MATERIALS AND METHODS

**Sample Preparation.** For amyloid fibril samples, bovine insulin (Sigma-Aldrich #I5500) was reconstituted to 5 mg/mL in 10 mM HCl.[34] This solution was incubated at 80 °C for 48 h. The fibril suspension was diluted to 0.5 mg/mL protein and was purified by 15 centrifugations at 3000$g$ for 1 min each to remove smaller aggregates. A 10 μL portion of a 0.05 mg/mL suspension was adsorbed onto freshly cleaved mica (EMS no. 71851-05) at room temperature for 1.5 min, followed by washing with copious amounts of Millipore-grade water. A stream of nitrogen was used to dry amyloid samples that were imaged in ambient air. Imaging was performed in air or in 1 mL Millipore water in a static fluid cell. Additional water was added as needed to compensate for evaporation.

**Instrumentation for the Measurements of Electromechanical Coupling.**
*Single Frequency Experiments.* Electromechanical coupling on amyloid and mica was measured using Asylum Research (Santa Barbara, CA) MFP3D atomic force microscope (AFM). External function generator (SR DS345) was used to bias the tip with AC bias of 10 V amplitude and single frequency from 100 to 200 kHz range. For each experiment a single frequency in the 100−200 kHz range was chosen to maximize the amplitude of mechanical response. The amplitude of mechanical response was measured by feeding vertical deflection signal from photodetector of the microscope into lock-in amplifier (SR844 RF). Au-coated tip (Olympus, RC800PB) with stiffness ∼0.06 N/m and resonance frequency of 17 kHz was used for the experiments. The cantilever had a spring-board shape with 20 μm width, 200 μm length, and 0.8 μm thickness. The experiment was an exact replica of PFM experiments done in air; ref 50 provides more details on the experiment configuration.

*Band Excitation Experiments.* PFM and band excitation[50] PFM was implemented on an Asylum Research (Santa Barbara, CA) MFP3D atomic force microscope (AFM) and an in-house developed Mat-Lab/LabView data acquisition and control system. A voltage excitation band spanning approximately 50−280 kHz (increasing chirp) with amplitude of 10 V was applied to the microscope tip. The mechanical response of the system was recorded by measuring and digitally storing the motion of the tip, taking the Fourier transform of the response. The amplitude, resonance frequency, and quality factor were extracted using a damped harmonic oscillator model at regular intervals during the tip biasing process. Au-coated tip (Olympus, RC800PB) with stiffness ∼0.06 N/m and resonance frequency of 17 kHz was used for the experiments. The cantilever had a spring-board shape with 20 μm width, 200 μm length, and 0.8 μm thickness.

## REFERENCES AND NOTES

1. Kalinin, S. V.; Setter, N.; Kholkin, A. L.,. Eds. Electromechanics on the Nanometer Scale: Emerging Phenomena, Devices, and Applications. *MRS Bull.* **2009**, *34*, 634.

2. Juluri, B. K.; Kumar, A. S.; Liu, Y.; Ye, T.; Yang, Y. W.; Flood, A. H.; Fang, L.; Stoddart, J. F.; Weiss, P. S.; Huang, T. J. A Mechanical Actuator Driven Electrochemically by Artificial Molecular Muscles. *ACS Nano* **2009**, *3*, 291–300.

3. Madden, J. D. Mobile Robots: Motor Challenges and Materials Solutions. *Science* **2007**, *318*, 1094–1097.

4. Shirai, Y.; Osgood, A. J.; Zhao, Y. M.; Yao, Y. X.; Saudan, L.; Yang, H. B.; Chiu, Y. H.; Alemany, L. B.; Sasaki, T.; Morin, J. F.; *et al*. Surface-Rolling Molecules. *J. Am. Chem. Soc.* **2006**, *128*, 4854–4864.

5. *International Technology Roadmap for Semiconductors*; 2008. http://www.itrs.net/reports.html.

6. Balzani, V.; Credi, A.; Venturi, M. Light Powered Molecular Machines. *Chem. Soc. Rev.* **2009**, *38*, 1542–1550.

7. Ferris, D. P.; Zhao, Y. L.; Khashab, N. M.; Khatib, H. A.; Stoddart, J. F.; Zink, J. I. Light-Operated Mechanized Nanoparticles. *J. Am. Chem. Soc.* **2009**, *131*, 1686–1688.

8. Kim, H.; Goddard, W. A.; Jang, S. S.; Dichtel, W. R.; Heath, J. R.; Stoddart, J. F. Free Energy Barrier for Molecular Motions in Bistable ²Rotaxane Molecular Electronic Devices. *J. Phys. Chem. A* **2009**, *113*, 2136–2143.

9. Zheng, Y. B.; Yang, Y. W.; Jensen, L.; Fang, L.; Juluri, B. K.; Flood, A. H.; Weiss, P. S.; Stoddart, J. F.; Huang, T. J. Active Molecular Plasmonics: Controlling Plasmon Resonances with Molecular Switches. *Nano Lett.* **2009**, *9*, 819–825.

10. Kumar, A. S.; Ye, T.; Takami, T.; Yu, B. C.; Flatt, A. K.; Tour, J. M.; Weiss, P. S. Reversible Photo-Switching of Single Azobenzene Molecules in Controlled Nanoscale Environments. *Nano Lett.* **2008**, *8*, 1644–1648.

11. Moore, A. M.; Mantooth, B. A.; Donhauser, Z. J.; Yao, Y. X.; Tour, J. M.; Weiss, P. S. Real-Time Measurements of Conductance Switching and Motion of Single Oligo(phenylene ethynylene) Molecules. *J. Am. Chem. Soc.* **2007**, *129*, 10352–10353.

12. Soong, R.; Montemagno, C. D. Engineering Hybrid Nano-Devices Powered by the F-1-ATPase Biomolecular Motor. *Int. J. Nanotechnol.* **2005**, *2*, 371–396.

13. Choi, H. J.; Montemagno, C. D. Artificial Organelle: ATP Synthesis from Cellular Mimetic Polymersomes. *Nano Lett.* **2005**, *5*, 2538–2542.

14. Butt, H. J. Towards Powering Nanometer-Scale Devices with Molecular Motors: Single Molecule Engines. *Macromol. Chem. Phys.* **2006**, *207*, 573–575.

15. Browne, W. R.; Feringa, B. L. Making Molecular Machines Work. *Nat. Nanotechnol.* **2006**, *1*, 25–35.

16. Rescifina, A.; Zagni, C.; Iannazzo, D.; Merino, P. Recent Developments on Rotaxane-Based Shuttles. *Curr. Org. Chem.* **2009**, *13*, 448–481.

17. Gong, X. J.; Li, J. Y.; Lu, H. J.; Wan, R. Z.; Li, J. C.; Hu, J.; Fang, H. P. A Charge-Driven Molecular Water Pump. *Nat. Nanotechnol.* **2007**, *2*, 709–712.

18. Yamaki, M.; Hoki, K.; Teranishi, T.; Chung, W. C.; Pichierri, F.; Kono, H.; Fujimura, Y. Theoretical Design of an Aromatic Hydrocarbon Rotor Driven by a Circularly Polarized Electric Field. *J. Phys. Chem. A* **2007**, *111*, 9374–9378.

19. Flood, A. H.; Ramirez, R. J. A.; Deng, W. Q.; Muller, R. P.; Goddard, W. A.; Stoddart, J. F. Meccano on the Nanoscale—A Blueprint for Making Some of the World's Tiniest Machines. *Aust. J. Chem.* **2004**, *57*, 301–322.

20. Horinek, D.; Michl, J. Molecular Dynamics Simulation of an Electric Field Driven Dipolar Molecular Rotor Attached to a Quartz Glass Surface. *J. Am. Chem. Soc.* **2003**, *125*, 11900–11910.

21. Vacek, J.; Michl, J. Molecular Dynamics of a Grid-Mounted Molecular Dipolar Rotor in a Rotating Electric Field. *Proc. Natl. Acad. Sci. U.S.A.* **2001**, *98*, 5481–5486.

22. Noy, A. *Handbook of Molecular Force Spectroscopy*; Springer: New York, 2007.

23. Gruverman, A.; Kholkin, A. Nanoscale Ferroelectrics: Processing, Characterization and Future Trends. *Rep. Prog. Phys.* **2006**, *69*, 2443–2474.

24. Nikolaeva, E. V.; Shur, V. Y.; Shishkin, E. I.; Sternberg, A. In *Nanoscale Domain Structure in Relaxor PLZT x/65/35 Ceramics*, International Symposium on Micro- and Nano-Scale Domain Structuring Ferroelectrics (ISDS 2005), Ekaterinburg, RUSSIA, Nov 15−19, 2005; Taylor & Francis Ltd: Ekaterinburg, Russia, 2005; pp 137−143.

25. Rodriguez, B. J.; Jesse, S.; Baddorf, A. P.; Kalinin, S. V. High Resolution Electromechanical Imaging of Ferroelectric Materials in a Liquid Environment by Piezoresponse Force Microscopy. *Phys. Rev. Lett.* **2006**, *96*, 237602.

26. Calarco, R.; Meijers, R.; Stoica, T.; Luth, H. In *Piezoresponse Force Microscopy for Imaging of GaN Surfaces*, International Workshop on Nitrides Semiconductors (IWN 2004), Pittsburgh, PA, Jul 19−23, 2004; Wiley-VCH Verlag Gmbh: Pittsburgh, PA, 2004; pp 785−789.

27. Bdikin, I. K.; Shvartsman, V. V.; Kholkin, A. L. In *Nanoscale Ferroelectric Properties of PZN-PT Single Crystals Studied by Scanning Force Microscopy*, Symposium on Materials and Devices for Smart Systems held at the 2003 MRS Fall Meeting, Boston, MA, Dec 01−05, 2003; Furuya, Y.; Quandt, E.; Zhang, Q.; Inoue, K.; Shahinpoor, M., Eds. Materials Research Society: Boston, MA, 2003; pp 147−152.

28. Tybell, T.; Paruch, P.; Giamarchi, T.; Triscone, J. M. Domain Wall Creep in Epitaxial Ferroelectric Pb(Zr$_{0.2}$Ti$_{0.8}$)O$_3$ Thin Films. *Phys. Rev. Lett.* **2002**, *89*, 097601.

29. Paruch, P.; Giamarchi, T.; Triscone, J. M. In *Domain Wall Creep in Mixed c−a axis Pb(Zr0.2Ti0.8)O-3 Thin Films*, 10th International Workshop on Oxide Electronics, Augsbaurg, Germany, Sep 11−13, 2003; Wiley-VCH Verlag Gmbh: Augsbaurg, Germany, 2003; pp 95−96.

30. Maksymovych, P.; Jesse, S.; Huijben, M.; Ramesh, R.; Morozovska, A.; Choudhury, S.; Chen, L. Q.; Baddorf, A. P.; Kalinin, S. V. Intrinsic Nucleation Mechanism and Disorder Effects in Polarization Switching on Ferroelectric Surfaces. *Phys. Rev. Lett.* **2009**, *102*, 017601.

31. Jesse, S.; Rodriguez, B. J.; Choudhury, S.; Baddorf, A. P.; Vrejoiu, I.; Hesse, D.; Alexe, M.; Eliseev, E. A.; Morozovska, A. N.; Zhang, J.; *et al*. Direct Imaging of the Spatial and Energy Distribution of Nucleation Centres in Ferroelectric Materials. *Nat. Mater.* **2008**, *7*, 209–215.

32. Kalinin, S. V.; Rodriguez, B. J.; Jesse, S.; Thundat, T.; Gruverman, A. Electromechanical Imaging of Biological Systems with sub-10 nm Resolution. *Appl. Phys. Lett.* **2005**, *87*, 053901.

33. Rodriguez, B. J.; Jesse, S.; Baddorf, A. P.; Kim, S. H.; Kalinin, S. V. Controlling Polarization Dynamics in a Liquid Environment: From Localized to Macroscopic Switching in Ferroelectrics. *Phys. Rev. Lett.* **2007**, *98*, 247603.

34. Guo, S. L.; Akhremitchev, B. B. Packing Density and Structural Heterogeneity of Insulin Amyloid Fibrils Measured by AFM Nanoindentation. *Biomacromolecules* **2006**, *7*, 1630–1636.

35. Guo, S.; Akhremitchev, B. B. Investigation of Mechanical Properties of Insulin Crystals by Atomic Force Microscopy. *Langmuir* **2008**, *24*, 880–887.

36. Jansen, R.; Dzwolak, W.; Winter, R. Amyloidogenic Self-Assembly of Insulin Aggregates Probed by High Resolution Atomic Force Microscopy. *Biophys. J.* **2005**, *88*, 1344–1353.

37. Knowles, T. P.; Fitzpatrick, A. W.; Meehan, S.; Mott, H. R.; Vendruscolo, M.; Dobson, C. M.; Welland, M. E. Role of Intermolecular Forces in Defining Material Properties of Protein Nanofibrils. *Science* **2007**, *318*, 1900–1903.

38. Knowles, T. P. J.; Smith, J. F.; Craig, A.; Dobson, C. M.; Welland, M. E. Spatial Persistence of Angular Correlations in Amyloid Fibrils. *Phys. Rev. Lett.* **2006**, *96*, 238301.

39. Smith, J. F.; Knowles, T. P. J.; Dobson, C. M.; MacPhee, C. E.; Welland, M. E. Characterization of the Nanoscale Properties of Individual Amyloid Fibrils. *Proc. Natl. Acad. Sci. U.S.A.* **2006**, *103*, 15806–15811.

40. Sunde, M.; Serpell, L. C.; Bartlam, M.; Fraser, P. E.; Pepys, M. B.; Blake, C. C. F. Common Core Structure of Amyloid Fibrils by Synchrotron X-ray Diffraction. *J. Mol. Biol.* **1997**, *273*, 729–739.

41. Geddes, A. J.; Parker, K. D.; Atkins, E. D. T.; Beighton, E. Cross-Beta Conformation in Proteins. *J. Mol. Biol.* **1968**, *32*, 343–344.

42. Kyle, R. A. Amyloidosis: A Convoluted Story. *Br. J. Hamaetol.* **2001**, *114*, 529–538.

43. Sipe, J. D.; Cohen, A. S. Review: History of the Aamyloid Fibril. *J. Struct. Biol.* **2000**, *130*, 88–98.

44. Grudzielanek, S.; Jansen, R.; Winter, R. Solvational Tuning of the Unfolding, Aggregation, and Amyloidogenesis of Insulin. *J. Mol. Biol.* **2005**, *351*, 879–894.

45. Swift, B.; Hawkins, P. N.; Richards, C.; Gregory, R. Examination of Insulin Injection Sites: An Unexpected Finding of Localized Amyloidosis. *Diabetic Med.* **2002**, *19*, 881–882.

46. Storkel, S.; Schneider, H. M.; Muntefering, H.; Kashiwagi, S. Iatrogenic, Insulin-Dependent, Local Amyloidosis. *Lab. Invest.* **1983**, *48*, 108–111.

47. Gasparini, L.; Dityatev, A. Beta-Amyloid and Glutamate Receptors. *Exp. Neurol.* **2008**, *212*, 1–4.

48. Glenner, G. G.; Wong, C. W. Alzheimers-Disease and Downs-Syndrome—Sharing of a Unique Cerebrovascular Amyloid Fibril Protein. *Biochem. Biophys. Res. Co.* **1984**, *122*, 1131–1135.

49. Proksch, R.; Kalinin, S. V. Piezoresponse Force Microscopy with Asylum Research AFM. *http://www.asylumresearch.com/Applications/PFMAppNote/PFMAppNote.shtml*, 2009.

50. Jesse, S.; Kalinin, S. V.; Proksch, R.; Baddorf, A. P.; Rodriguez, B. J. The Band Excitation Method in Scanning Probe Microscopy for Rapid Mapping of Energy Dissipation on the Nanoscale. *Nanotechnology* **2007**, *18*, 435503.

51. Jesse, S.; Mirman, B.; Kalinin, S. V. Resonance Enhancement in Piezoresponse Force Microscopy: Mapping Electromechanical Activity, Contact Stiffness, and Q Factor. *Appl. Phys. Lett.* **2006**, *89*, 022906.

52. Kalinin, S. V.; Karapetian, E.; Kachanov, M. Nanoelectromechanics of Piezoresponse Force Microscopy. *Phys. Rev. B* **2004**, *70*, 24.

53. Rabe, U.; Janser, K.; Arnold, W. Vibrations of Free and Surface-Coupled Atomic Force Microscope Cantilevers: Theory and Experiment. *Rev. Sci. Instrum.* **1996**, *67*, 3281–3293.

54. Hirsekorn, S.; Rabe, U.; Arnold, W. Theoretical Description of the Transfer of Vibrations from a Sample to the Cantilever of an Atomic Force Microscope. *Nanotechnology* **1997**, *8*, 57–66.

55. Kalinin, S. V.; Rodriguez, B. J.; Jesse, S.; Seal, K.; Proksch, R.; Hohlbauch, S.; Revenko, I.; Thompson, G. L.; Vertegel, A. A. Towards Local Electromechanical Probing of Cellular and Biomolecular Systems in a Liquid Environment. *Nanotechnology* **2007**, *18*, 424020.

56. Jesse, S.; Kalinin, S. V. Principal Component and Spatial Correlation Analysis of Spectroscopic-Imaging Data in Scanning Probe Microscopy. *Nanotechnology* **2009**, *20*, 085714.

57. Bonnet, N. Some Trends in Microscope Image Processing. *Micron* **2004**, *35*, 635–653.

58. Bosman, M.; Watanabe, M.; Alexander, D. T. L.; Keast, V. J. Mapping Chemical and Bonding Information Using Multivariate Analysis of Electron Energy-Loss Spectrum Images. *Ultramicroscopy* **2006**, *106*, 1024–1032.

ARTICLE

59. Kracke, B.; Damaschke, B. Measurement of Nanohardness and Nanoelasticity of Thin Gold Films with Scanning Force Microscope. *Appl. Phys. Lett.* **2000**, *77*, 361–363.

60. Tagantsev, A. K. Piezoelectricity and Flexoelectricity in Crystalline Dielectrics. *Phys. Rev. B* **1986**, *34*, 5883–5889.

61. Minary-Jolandan, M.; Yu, M. F. Uncovering Nanoscale Electromechanical Heterogeneity in the Subfibrillar Structure of Collagen Fibrils Responsible for the Piezoelectricity of Bone. *ACS Nano* **2009**, *3*, 1859.

62. Kacprzyk, R.; Dobrucki, A.; Gajewski, J. B. Double-Layer Electret Transducer. *J. Electrostat.* **1997**, *39*, 33–40.

63. Sessler, G. M.; Hillenbrand, J. Electromechanical Response of Cellular Electret Films. *Appl. Phys. Lett.* **1999**, *75*, 3405–3407.

64. Sessler, G. M.; Hillenbrand, J. In *Electromechanical Response of Cellular Electret Films*, 10th International Symposium on Electrets, 1999; IEEE Service Center: 1999.

65. Kalinin, S. V.; Rar, A.; Jesse, S. A Decade of Piezoresponse Force Microscopy: Progress, Challenges, and Opportunities. *IEEE Trans. Ultrason. Ferr.* **2006**, *53*, 2226–2252.

66. Jesse, S.; Nikiforov, M. P.; Germinario, L. T.; Kalinin, S. V. Local Thermomechanical Characterization of Phase Transitions Using Band Excitation Atomic Force Acoustic Microscopy with Heated Probe. *Appl. Phys. Lett.* **2008**, *93*, 073104.

67. R.A., F. J. *Nanomedicine, Vol. I: Basic Capabilities*; Landes Bioscience: Austin, TX, 1999.

68. Leary, S. P.; Liu, C. Y.; Apuzzo, M. L. I. Toward the Emergence of Nanoneurosurgery: Part III—Nanomedicine: Targeted Nanotherapy, Nanosurgery, and Progress toward the Realization of Nanoneurosurgery. *Neurosurgery* **2006**, *58*, 1009–1025.

69. Sauer, C.; Stanacevic, M.; Cauwenberghs, G.; Thakor, N. Power Harvesting and Telemetry in CMOS for Implanted Devices. *IEEE Trans. Circuits Syst.* **2005**, *52*, 2605–2613.

70. Kumar, M. Nano and Microparticles as Controlled Drug Delivery Devices. *J. Pharm. Pharm. Sci.* **2000**, *3*, 234–258.